IOP Publishing Journal of Micromechanics and Microengineering
J. Micromech. Microeng. **27** (2017) 045017 (12pp) https://doi.org/10.1088/1361-6439/aa62b3

The electromechanical behavior of piezoelectric thin film composite diaphragms possessing in-plane stresses

B A Griffin[1], M D Williams[1], G Wang[2], B V Sankar[3], L N Cattafesta[4] and M Sheplak[5]

[1] Sandia National Laboratories, Albuquerque, NM 87185, United States of America
[2] MEMS Drive, Pasadena, CA 91107, United States of America
[3] Department of Mechanical and Aerospace Engineering, University of Florida, Gainesville, FL 32611-6250, United States of America
[4] Department of Mechanical Engineering, Florida State University, Tallahassee, FL 32310-6046, United States of America
[5] Department of Mechanical and Aerospace Engineering, Interdisciplinary Microsystems Group, University of Florida, Gainesville, FL 32611-6250, United States of America

E-mail: sheplak@ufl.edu

Received 19 September 2016, revised 18 February 2017
Accepted for publication 24 February 2017
Published 14 March 2017

Abstract

Many piezoelectric microelectromechanical systems (MEMS) measure or generate acoustic signals via the motion of radially non-uniform, thin film composite plates. The composite layers provide piezoelectric actuation, structural support, electrode metallization, passivation, etc. Often, the layers are non-uniform over the plate and contain residual stresses introduced during the fabrication process. Accurate models of non-uniform composite plate mechanics are crucial for predicting and optimizing device performance. In this paper, an analytical solution for a radially non-uniform, piezoelectric, circular composite plate incorporating residual stress is derived. The analytical solution is compared to experimental measurements of a MEMS piezoelectric diaphragm. The results show the improved accuracy of the analytical model when including film stress, the speed of the analytical solution as compared to finite element analysis, the sensitivity of device performance to residual stress and the importance of accurate film stresses as model inputs. The analytical model presented is useful as a design optimization tool given the efficiency of the computational time, shown to be 275 times less than a comparable finite element analysis.

Keywords: piezoelectric micromachined ultrasonic transducer, composite plate, piezoelectric diaphragm

(Some figures may appear in colour only in the online journal)

1. Introduction

Piezoelectric composite diaphragms are widely used in MEMS, with reported applications in energy harvesters [1], accelerometers [2, 3], micropumps [4, 5] piezoelectric micromachined ultrasonic transducers (PMUTs) [6–9] and microphones [10–16]. Rectangular [4, 8, 10–12] or circular diaphragm [1–3, 6, 7, 9, 13–16] constructions are common, and depending on their application can have uniform or non-uniform layer compositions. In circular unimorph (one piezoelectric layer) and bimorph (two piezoelectric layers) geometries, the piezoelectric layers and/or electrodes often do

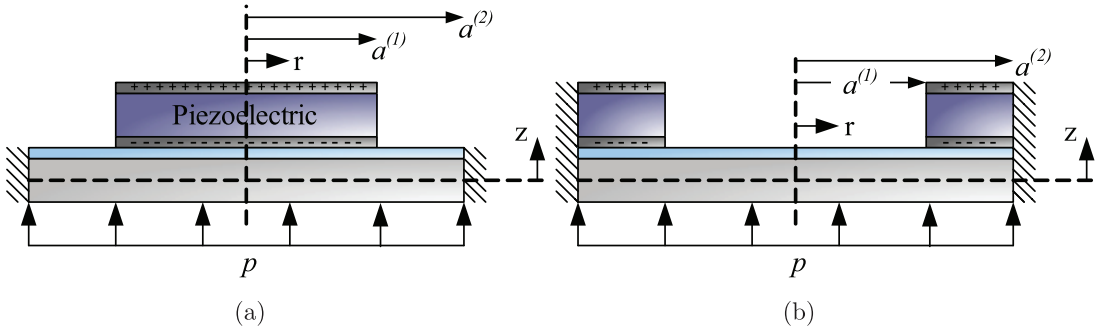

Figure 1. Example piezoelectric composite unimorph diaphragm geometries utilized in microsystems (not to scale). (a) Radially non-uniform circular unimorph. (b) Radially non-uniform annular unimorph.

not extend over the whole of the diaphragm. Two example unimorph geometries commonly utilized in microscale devices are illustrated in figure 1.

These diaphragms are formed from piezoelectric films together with a host of other materials in a composite layup. The supporting materials typically include metal or polysilicon electrodes, isolating silicon dioxide, and structural silicon or silicon nitride layers. In-plane residual stresses are nearly omnipresent byproducts of microfabrication processes and often dominate the behavior of these thin-film mechanical structures. Thermal expansion mismatch between films, substrate, and package lead to extrinsic thermal stress, while factors including lattice mismatch, impurities, volume change processes (e.g. phase transformation or outgassing), or atoms being trapped in high-energy configurations contribute to intrinsic stresses [17, 18]. Thus, a mechanical model of the piezoelectric composite diaphragm that accounts for residual in-plane stresses is critical for successful design of thin-film piezoelectric MEMS. Although this can be accomplished using finite element analysis, it is computationally costly making it non-ideal as a design optimization tool. In this paper, an analytical plate model for a radially non-uniform multi-layered axisymmetric piezoelectric diaphragm subjected to in-plane stresses, transverse pressure, and applied voltage is developed that is also computationally efficient in comparison to finite element analysis. The model was used in design optimization of aluminum nitride based PMUTs [9] and microphones [15, 16].

The literature on piezoelectric composite plates, even narrowed to unimorphs of circular geometry, is extensive. Analytical investigations of diaphragms with radially non-uniform layer composition as in figure 1 appear to have first been addressed by Antonyak and Vassergiser [19], who presented a static model of a simply-supported two-layer circular unimorph transducer in which the radius of the piezoelectric layer was less than that of the structural layer. The governing equations were solved piecewise on either side of the step discontinuity, with matching conditions on moments and displacements applied at the step discontinuity. An equivalent electroacoustic circuit was used to examine the variation of sensitivity and electromechanical coupling coefficient with changes in thickness and radius ratios. Evseichik *et al* [20] performed a similar study in 1991, but solved the time-harmonic governing equations. The impacts of clamped, free, and hinged boundary conditions were discussed. Later, Chang and Du [21] formally determined optimized configurations for large electromechanical coupling factors and static deflections.

A static model of a clamped piezoelectric circular plate with radially non-uniform layers together with a two-port electroacoustic equivalent circuit representation was developed in a series of conference and journal papers from the Interdisciplinary Microsystems Group at the University of Florida [22–24] in the years 2002–2006. In Prasad *et al* [23, 24], a compact, closed-form solution was offered for the problem of a clamped unimorph with a circular piezoelectric layer. Layer composition was generalized in the provided solution via use of the composite stiffness matrices, though the outer region was restricted to symmetric layups. The two-port electroacoustic equivalent circuit developed had the same form utilized by Antonyak and Vassergiser [19]. The model was validated experimentally and with finite element analysis [23]. Another version of the model presented in Wang *et al* [22] included in-plane residual stress as an input.

Ayela *et al* [25] later utilized the model to design buckled micromembranes and extract the d_{31} piezoelectric coefficient from interferometer measurements. In 2003, Li and Chen [26] found the deflection profile of a simply-supported unimorph with inner-disc actuator and bond layer. Later, several papers from a group at the University of Pittsburgh addressed circular piezoelectric unimorphs. In 2005, Kim *et al* [27] presented models for a circular unimorph with uniform piezoelectric and structural-layer thicknesses but two different electrode configurations. In the first configuration, the electrodes fully covered the piezoelectric layer; in the second, the electrodes were segmented into inner and outer regions with reversed polarization. In 2006, Mo *et al* [28] investigated a two layer unimorph with clamped, simply-supported, and elastic edge conditions. Both radially uniform and non-uniform layer compositions were discussed. The authors focused on the variation of deflection profiles with a number of parameters, including thickness, radius, and elastic modulus ratios of the piezoelectric to structural layer. Experimental verification was also provided. The next year, the same authors modified the model with a segmented electrode configuration [27] to include elastically-restrained edge conditions. Experimental verification of the model was provided [29].

Deshpande and Saggere [30] provided a generalized static model for prediction of the displacements of a circular piezoelectric plate with a single radial discontinuity. The ease of modeling arbitrary layer configurations via avoidance of early simplifications to the composite stiffness matrices was emphasized. Finite element and experimental verification were given for a range of voltage and pressure loadings. Papila *et al* [31]

provided a similarly general formulation for a circular piezoelectric plate with two radial discontinuities.

This paper builds on the prior conference publication [22]. It presents a substantially generalized static model for prediction of the displacement profile of an axisymmetric piezoelectric composite diaphragm with a single radial discontinuity and arbitrary layer composition, including prescription of layer residual stresses. The displacement response to both voltage and pressure loading is considered. Such a model may be used directly with the lumped element modeling technique [9, 15, 16, 23] to predict linear dynamic behavior. A comparison of model predictions with experimental measurements of a MEMS microphone diaphragm [15, 16] is also given.

This paper is organized into four sections. In the following section, the solution strategy is discussed and the governing equations for the piezoelectric composite plate are derived and solved in a generalized manner. In section 3, the model is compared with experimental results from a MEMS piezoelectric diaphragm. Section 4 concludes with final observations and suggestions for future work.

2. Composite plate model

The basic piezoelectric composite plate geometries modeled herein are found in figure 1, where the layer compositions are regarded as arbitrary. Because the layup of thin films is not radially uniform, the governing equations are solved in two domains, to be referred to as the inner circular region ($0 \leqslant r \leqslant a^{(1)}$) and the outer annular region ($a^{(1)} \leqslant r \leqslant a^{(2)}$). In this section, the governing differential equations for the piezoelectric composite plate will be derived; general analytical solutions for the transverse and radial displacements in each region will be obtained; and matching conditions at the interface between the two regions and boundary conditions will be used to determine the constants of integration.

2.1. Solution technique

A radially uniform piezoelectric composite plate with a biaxial state of residual stress is pictured in figure 2(a). A perfectly clamped plate such as this does not displace under the action of in-plane residual stress. However, a discontinuity in stress introduced via radial non-uniformity as in figure 2(b), induces a bending moment that causes displacement. In the case of an elastically restrained or simply-supported plate, a similar bending moment emerges at the plate boundary. Meanwhile, plate displacement resulting from the converse piezoelectric reaction to an applied voltage in a radially non-uniform piezocomposite occurs in much the same way, with a voltage induced in-plane stress producing an effective bending moment. Thus, under voltage loading or external pressure loading, additional displacement results as in figure 2(c).

In the design of microfabricated piezoelectric devices, the incremental displacement of figure 2(c) due to external loads is of primary importance, for example as an input to a predictive lumped element model [9, 13, 15, 16, 23]. In this work, incremental displacement is found from

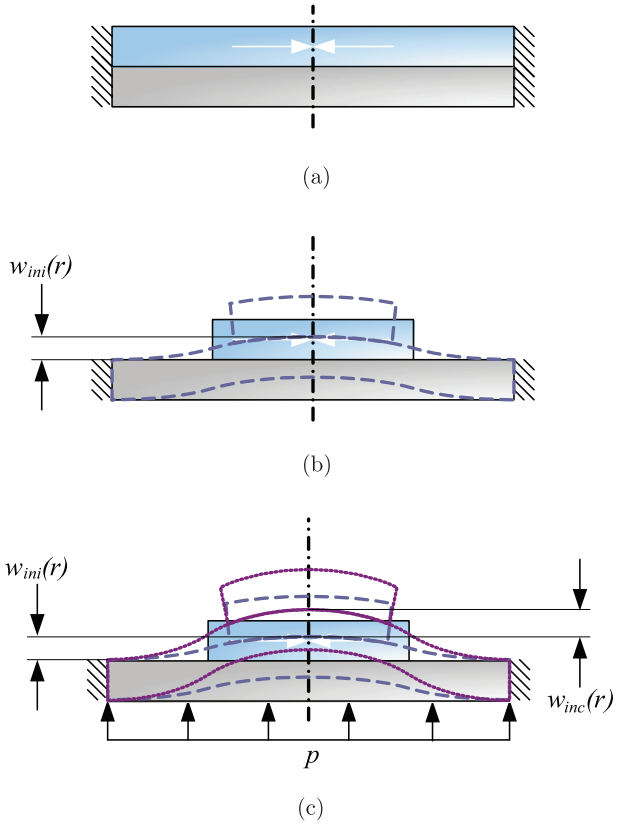

Figure 2. Comparison of initial displacements between uniform (a) and non-uniform composite plates (b) and definition of incremental deflection due to loading (c). (a) Perfectly clamped plate with radially uniform layers and in-plane stress has no initial deflection. (b) Etched structure exhibits initial deflection due to in-plane residual stress. (c) Incremental deflection due to pressure (or voltage) loading.

$$w_{\text{inc}}(r) = w_{\text{tot}}(r) - w_{\text{ini}}(r) = w(r)\big|_{\sigma_0 \neq 0, P|V \neq 0} - w(r)\big|_{\sigma_0 \neq 0, P|V=0}, \tag{1}$$

where the first term on the right hand side is the total displacement due to both in-plane residual stress and external loading, and the second term is the initial displacement due solely to in-plane residual stress. The goal, then, is to derive a predictive model for the geometries of figure 1 with inputs representing in-plane residual stress, pressure, and applied voltage. Clearly, for a plate with zero in-plane stress, $w_{\text{inc}} = w_{\text{tot}}$.

2.2. Axisymmetric model derivation

A list of variables used through the following derivation is given in table 1 for convenience. Figure 3 should be referenced for coordinate conventions.

2.2.1. Strain-displacement relations. Under the assumption of *small, finite deformations*, the kinematic assumptions of Kirchhoff plate theory allow the strain field in an axisymmetric plate to be reduced to [32]

$$\boldsymbol{\varepsilon} = \boldsymbol{\varepsilon}^{\mathbf{0}} + z\boldsymbol{\kappa}, \tag{2}$$

Table 1. Variables definitions for the axisymmetric model derivation.

Variable	Description
r, θ, z	Cylindrical coordinates
u,w	Deflection in the r and z directions, respectively
$\boldsymbol{\varepsilon}$	Strain vector
$\boldsymbol{\varepsilon^0}$	Strain vector at surface $z = 0$
$\boldsymbol{\kappa}$	Curvature strain vector
$\boldsymbol{N}$	Force resultant vector
$\boldsymbol{M}$	Moment resultant vector
Q_r	Radial shear force resultant
p	Pressure
$z_0 \ldots z_N$	Coordinates of the composite layers
$\boldsymbol{\sigma}$	Stress vector
$\boldsymbol{\sigma_0}$	Fabrication-induced biaxial stress vector
d_{31}	Piezoelectric constant relating normal electric field to in-plane strains
E_f	Electric field
$\boldsymbol{Q}$	Reduced stiffness matrix for a transversely isotropic material
$\boldsymbol{A}, \boldsymbol{B}, \boldsymbol{D}$	Extensional, flexural-extensional, and flexural stiffness matrices, respectively
$\boldsymbol{N_0}, \boldsymbol{M_0}$	Fabrication-induced force and moment resultant vectors
$\boldsymbol{N_P}, \boldsymbol{M_P}$	Piezoelectric induced force and moment resultant vectors
ϕ	In-plane rotation, $\phi = -\mathrm{d}w/\mathrm{d}r$
D_{11}^*	Effective stiffness component, $D_{11}^* = D_{11} - B_{11}^2/A_{11}$
B_{12}^*	Effective stiffness component, $B_{12}^* = B_{12} - B_{11}A_{12}/A_{11}$
$\tilde{N}_r$	Strain-dependent component of N_r
x	Net sense of in-plane force parameter, $= \mathrm{sgn}(N_0)$
k^{*2}	Non-dimensional in-plane force parameter, $= \lvert N_0 \rvert \frac{a^2}{D_{11}^*}$
J_n, Y_n	nth order bessel function of the first and second kind, respectively
I_n, K_n	nth order modified bessel function of the first and second kind, respectively
$a^{(1)}, a^{(2)}$	Inner and outer radii of the annulus, respectively
$\boldsymbol{C_i^j}^T$	Array which contains the coefficients of the integration constants
$\boldsymbol{c^{(j)}}$	Integration constants
$\boldsymbol{f_i^{(j)}}$	Forcing functions

where $\boldsymbol{\varepsilon} = \{\varepsilon_{rr}\ \varepsilon_{\theta\theta}\}^T$ collects the non-zero components of the reduced Green strain tensor. The so-called reference plane strains of the surface $z = 0$ are

$$\boldsymbol{\varepsilon^0} = \begin{Bmatrix} \varepsilon_r^0 \\ \varepsilon_\theta^0 \end{Bmatrix} = \begin{Bmatrix} \dfrac{\mathrm{d}u}{\mathrm{d}r} + \dfrac{1}{2}\left(\dfrac{\mathrm{d}w}{\mathrm{d}r}\right)^2 \\ \dfrac{u(r)}{r} \end{Bmatrix}, \tag{3}$$

and the curvatures are given as

$$\boldsymbol{\kappa} = \begin{Bmatrix} \kappa_r \\ \kappa_\theta \end{Bmatrix} = \begin{Bmatrix} \dfrac{\mathrm{d}^2 w}{\mathrm{d}r^2} \\ \dfrac{1}{r}\dfrac{\mathrm{d}w}{\mathrm{d}r} \end{Bmatrix}. \tag{4}$$

With the inclusion of the nonlinear term containing $(\mathrm{d}w/\mathrm{d}r)^2$ in (3), (2)–(4) collectively define the von Kármán strains [32].

2.2.2. Equilibrium equations. The equilibrium equations for the axisymmetric bending of a circular or annular plate are well-known [32, 33] to be

$$\frac{\mathrm{d}N_r}{\mathrm{d}r} + \frac{N_r(r) - N_\theta(r)}{r} = 0, \tag{5}$$

$$\frac{\mathrm{d}M_r}{\mathrm{d}r} + \frac{M_r(r) - M_\theta(r)}{r} + Q_r(r) = 0, \tag{6}$$

and

$$Q_r(r) = \frac{pr}{2} + N_r(r)\frac{\mathrm{d}w}{\mathrm{d}r}, \tag{7}$$

subject to essential or natural boundary conditions on u or N_r, $\mathrm{d}w/\mathrm{d}r$ or M_r, and w or $Q_r + N_r\mathrm{d}w/\mathrm{d}r$. The radial and circumferential force and moment resultants, grouped as $\boldsymbol{N} = \{N_r\ N_\theta\}^T$, $\boldsymbol{M} = \{M_r\ M_\theta\}^T$, respectively, are defined as

$$\boldsymbol{N} = \int_{z_0}^{z_N} \boldsymbol{\sigma}\mathrm{d}z \tag{8}$$

and

$$\boldsymbol{M} = \int_{z_0}^{z_N} \boldsymbol{\sigma} z\mathrm{d}z, \tag{9}$$

where $\boldsymbol{\sigma} = \{\sigma_{rr}\ \sigma_{\theta\theta}\}^T$.

2.2.3. Constitutive equation. To form governing equilibrium equations in terms of displacements, the stresses (and thus in-plane forces and moments) must be related to the strains (and thus displacements) via the elastic constitutive equations. The linear piezoelectric effect is also included at this stage. The plane strain constitutive equations for the axisymmetric, linearly elastic circular plate are

$$\boldsymbol{\sigma} = \boldsymbol{\sigma_0} + \boldsymbol{Q}(\boldsymbol{\varepsilon} - \boldsymbol{d}E_f), \tag{10}$$

where $\boldsymbol{\sigma_0} = \{\sigma_0\ \sigma_0\}^T$ represents the assumed biaxial state of stress resulting from the fabrication process, $\boldsymbol{d} = \{d_{31}\ d_{31}\}^T$, d_{31} is the piezoelectric constant relating an electric field in the z-direction to strains in the plane of the plate, E_f is an applied electric field, and the reduced stiffness matrix $\boldsymbol{Q}$ for a transversely isotropic material takes the form

$$\boldsymbol{Q} = \frac{E_r}{1 - \nu_{r\theta}^2}\begin{bmatrix} 1 & \nu_{r\theta} \\ \nu_{r\theta} & 1 \end{bmatrix}, \tag{11}$$

where the subscripts on the elastic modulus E and Poisson ratio ν are included to clarify the directionality of the material properties, but are henceforth dropped for convenience. The

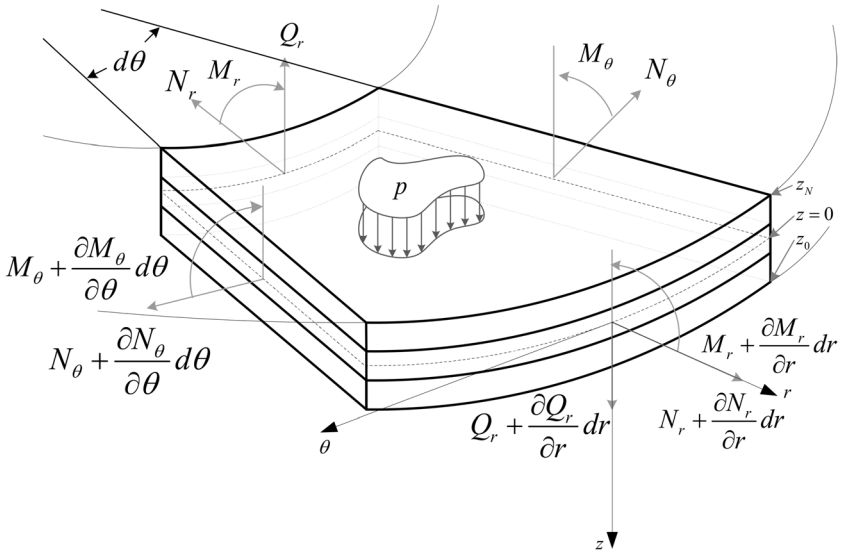

Figure 3. Coordinate convention for forces and moments used in the axisymmetric model derivation.

material properties and electric field are considered constant in each layer and thus piecewise constant through the thickness of the plate. With this in mind, integrating (10) through the plate yields the well-known constitutive equations of a piezoelectric composite plate,

$$\begin{Bmatrix} \boldsymbol{N} \\ \boldsymbol{M} \end{Bmatrix} = \begin{Bmatrix} \boldsymbol{N_0} \\ \boldsymbol{M_0} \end{Bmatrix} + \begin{bmatrix} \boldsymbol{A} & \boldsymbol{B} \\ \boldsymbol{B} & \boldsymbol{D} \end{bmatrix} \begin{Bmatrix} \boldsymbol{\varepsilon} \\ \boldsymbol{\kappa} \end{Bmatrix} - \begin{Bmatrix} \boldsymbol{N_p} \\ \boldsymbol{M_p} \end{Bmatrix}, \tag{12}$$

where $\boldsymbol{A}$, $\boldsymbol{B}$, and $\boldsymbol{D}$ are the 2×2 extensional, flexural-extensional coupling, and flexural stiffness matrices, respectively. They are defined as

$$\{\boldsymbol{A}, \boldsymbol{B}, \boldsymbol{D}\} = \int_{z_0}^{z_N} \boldsymbol{Q}\{1, z, z^2\} \mathrm{d}z. \tag{13}$$

The in-plane force and moment as well as the effective piezoelectric force and moment are also defined as $\boldsymbol{N_0} = \{N_0\ N_0\}^T$, $\boldsymbol{M_0} = \{M_0\ M_0\}^T$, $\boldsymbol{N_p} = \{N_p\ N_p\}^T$ and $\boldsymbol{M_p} = \{M_p\ M_p\}^T$, respectively, where

$$\{N_0, M_0\} = \int_{z_0}^{z_N} \sigma_0\{1, z\} \mathrm{d}z \tag{14}$$

and

$$\{N_p, M_p\} = \int_{z_0}^{z_N} E_f d_{31} \frac{E}{1-\nu}\{1, z\} \mathrm{d}z. \tag{15}$$

In the latter equation, d_{31} is simply regarded as zero for non-piezoelectric material layers.

2.2.4. Governing differential equations. The governing equations expressed in mixed force-displacement form are found by first substituting the $\boldsymbol{N}$ and $\boldsymbol{M}$ components of (12) into (5) and the combination of (6) and (7), respectively. Canceling redundant terms in the two resulting equations yields

$$\frac{\mathrm{d}^2\phi}{\mathrm{d}r^2} + \frac{1}{r}\frac{\mathrm{d}\phi}{\mathrm{d}r} - \left(\frac{N_r(r)}{D_{11}^*} + \frac{1}{r^2}\right)\phi = -\frac{pr}{2D_{11}^*} + \frac{B_{12}^*}{2D_{11}^*}\frac{\phi^2}{r} \tag{16}$$

and

$$\frac{\mathrm{d}^2u}{\mathrm{d}r^2} + \frac{1}{r}\frac{\mathrm{d}u}{\mathrm{d}r} - \frac{u}{r^2} = -\frac{B_{11}}{A_{11}}\left(\frac{\mathrm{d}^2\phi}{\mathrm{d}r^2} + \frac{1}{r}\frac{\mathrm{d}\phi}{\mathrm{d}r} - \frac{\phi}{r^2}\right) - \left(\frac{1-A_{12}}{A_{11}}\right)\frac{\phi^2}{2r} - \phi\frac{\mathrm{d}\phi}{\mathrm{d}r}, \tag{17}$$

where ϕ is the in-plane rotation defined as

$$\phi = -\frac{\mathrm{d}w}{\mathrm{d}r}. \tag{18}$$

The effective stiffness components appearing in these equations are defined as $D_{11}^* = D_{11} - B_{11}^2/A_{11}$ and $B_{12}^* = B_{12} - B_{11}A_{12}/A_{11}$, where $B_{12}^* = 0$ for a symmetric laminate.

Equation (16) is nonlinear because of the products of the in-plane rotations, ϕ^2, as well as the multiplication of the unknown functions $N_r(r)$ and $\phi(r)$. A linearized form is sought next. First, let N_r be decomposed into components as

$$N_r = N_0 + \tilde{N}_r - N_p, \tag{19}$$

where $\tilde{N}_r$ is the strain-dependent component of N_r from (12). Substituting (19) into (16) yields

$$\frac{\mathrm{d}^2\phi}{\mathrm{d}r^2} + \frac{1}{r}\frac{\mathrm{d}\phi}{\mathrm{d}r} - \left(\frac{N_0 - N_p}{D_{11}^*} + \frac{1}{r^2}\right)\phi = -\frac{pr}{2D_{11}^*} + \frac{\phi\tilde{N}_r}{D_{11}^*} + \frac{B_{12}^*}{2D_{11}^*}\frac{\phi^2}{r}. \tag{20}$$

To linearize the governing equations, products of in-plane rotations are neglected in (17) and (20), as well as the $\phi\tilde{N}_r$ product in (20). In addition, there always exists a sufficiently small voltage input for which $N_p \ll N_0$, so N_p is removed from (20). The resulting linearized governing equations are

$$\frac{\mathrm{d}^2\phi}{\mathrm{d}r^2} + \frac{1}{r}\frac{\mathrm{d}\phi}{\mathrm{d}r} - \left(x\frac{k^{*2}}{a^2} + \frac{1}{r^2}\right)\phi = -\frac{pr}{2D_{11}^*}, \tag{21}$$

and

$$\frac{\mathrm{d}^2u}{\mathrm{d}r^2}+\frac{1}{r}\frac{\mathrm{d}u}{\mathrm{d}r}-\frac{u}{r^2}=-\frac{B_{11}}{A_{11}}\left(\frac{\mathrm{d}^2\phi}{\mathrm{d}r^2}+\frac{1}{r}\frac{\mathrm{d}\phi}{\mathrm{d}r}-\frac{\phi}{r^2}\right), \tag{22}$$

where x denotes the net sense of the in-plane force as

$$x=\mathrm{sgn}(N_0), \tag{23}$$

and k^{*2} is the non-dimensional in-plane force parameter,

$$k^{*2}=|N_0|\frac{a^2}{D_{11}^*}. \tag{24}$$

Equation (21) is consistent with the form of the equation for a homogeneous circular plate given in [34]. The presence of the k^{*2} term acts to make the stiffness of the plate dependent on the value of N_0.

2.2.5. General solutions. Equations (21) and (22) are valid in both the inner circular and outer annular regions of the plate. Both equations are non-homogeneous and they are sequentially coupled. Equation (21) is known as the modified Bessel equation when $x>0$, the Bessel equation when $x<0$, and the Cauchy equation when $x=0$. As a result, the solution of (21) has three different analytical forms,

$$\phi(r)=\begin{cases} c_1I_1\left(k^*\dfrac{r}{a}\right)+c_2K_1\left(k^*\dfrac{r}{a}\right)+\dfrac{1}{2}\dfrac{pa^2r}{D_{11}^*k^{*2}}, & x>0\\ c_1r+\dfrac{c_2}{r}-\dfrac{1}{16}\dfrac{pr^3}{D_{11}^*}, & x=0\\ c_1J_1\left(k^*\dfrac{r}{a}\right)+c_2Y_1\left(k^*\dfrac{r}{a}\right)-\dfrac{1}{2}\dfrac{pa^2r}{D_{11}^*k^{*2}}, & x<0, \end{cases} \tag{25}$$

which written in terms of w is

$$w(r)=\begin{cases} -c_1\dfrac{a}{k^*}I_0\left(k^*\dfrac{r}{a}\right)+c_2\dfrac{a}{k^*}K_0\left(k^*\dfrac{r}{a}\right)-\dfrac{1}{4}\dfrac{pa^2r^2}{D_{11}^*k^{*2}}+c_5, & x>0\\ -c_1\dfrac{1}{2}r^2-c_2\ln(r)+\dfrac{1}{64}\dfrac{pr^4}{D_{11}^*}+c_5, & x=0\\ c_1\dfrac{a}{k^*}J_0\left(k^*\dfrac{r}{a}\right)+c_2\dfrac{a}{k^*}Y_0\left(k^*\dfrac{r}{a}\right)+\dfrac{1}{4}\dfrac{pa^2r^2}{D_{11}^*k^{*2}}+c_5, & x<0. \end{cases} \tag{26}$$

Making use of (25) to resolve the right hand side of (17) and solving the resulting non-homogeneous Cauchy equation for all three values of x yields expressions for u,

$$u(r)=\begin{cases} c_3r+\dfrac{c_4}{r}-\dfrac{B_{11}}{A_{11}}\left[c_1I_1\left(k^*\dfrac{r}{a}\right)+c_2K_1\left(k^*\dfrac{r}{a}\right)\right], & x>0\\ c_3r+\dfrac{c_4}{r}+\dfrac{1}{16}\dfrac{B_{11}}{A_{11}}\dfrac{pr^3}{D_{11}^*}, & x=0\\ c_3r+\dfrac{c_4}{r}-\dfrac{B_{11}}{A_{11}}\left[c_1J_1\left(k^*\dfrac{r}{a}\right)+c_2Y_1\left(k^*\dfrac{r}{a}\right)\right], & x<0, \end{cases} \tag{27}$$

In (25)–(27), J and Y are Bessel functions of the first and second kind, respectively, and I and K are modified Bessel functions of the first and second kind. Their subscripts denote the order of the Bessel function. The solutions for u and w contain five integration constants c_1 through c_5. Solving these equations in the inner ($0\leqslant r\leqslant a^{(1)}$) and outer ($a^{(1)}\leqslant r\leqslant a^{(2)}$) domains demands ten constants be determined using boundary and matching conditions.

2.2.6. Boundary and matching conditions. To determine the constants, five boundary conditions and five matching conditions are employed. The first boundary conditions enforce symmetry and are

$$\phi^{(1)}(0)=0 \tag{28}$$

and

$$u^{(1)}(0)=0. \tag{29}$$

In each boundary condition above, the superscript $^{(i)}$ communicates that the quantity is evaluated in the ith region ($i=1,2$). Therefore, when these conditions are applied, any region-dependent input parameters found in (25) and (26), including all A, B, and D components, in addition to k^* and a, must be referenced to the appropriate plate region. Together, (28) and (29) immediately require that $c_2^{(1)}=c_4^{(1)}=0$ (with the same superscript convention applying to integration constants as input parameters) for all values of $x^{(1)}$. Eight integration constants remain and thus eight more boundary conditions are required. Additional boundary conditions on the outer plate edge are

$$M_r^{(1)}(a^{(2)})=-k_\phi\phi^{(2)}(a^{(2)}) \tag{30}$$

$$u^{(2)}(a^{(2)})=0, \tag{31}$$

and

$$w^{(2)}(a^{(2)})=0. \tag{32}$$

Equations (31) and (32) are classic clamped boundary conditions, while (30) is a compliant boundary condition which effectively makes the simply-supported ($k_\phi=0$) and clamped ($k_\phi=\infty$) cases available from the final solution.

The five remaining conditions require continuity of rotations, displacements, forces, and moments at the interface between the inner and outer regions ($r=a^{(1)}$) of the plate. They are

$$\phi^{(1)}(a^{(1)})=\phi^{(2)}(a^{(1)}), \tag{33}$$

$$u^{(1)}(a^{(1)})=u^{(2)}(a^{(1)}), \tag{34}$$

$$w^{(1)}(a^{(1)})=w^{(2)}(a^{(1)}), \tag{35}$$

$$N_r^{(1)}(a^{(1)})=N_r^{(2)}(a^{(1)}), \tag{36}$$

and

$$M_r^{(1)}(a^{(1)})=M_r^{(2)}(a^{(1)}). \tag{37}$$

Equations (37) and (36) require expressions for the radial moment and force, M_r and N_r, respectively. They are found from plugging (26) and (27) into (3) and (4) and the result into (12). The final force and moment expressions are

$$N_r(r) = \begin{cases} N_0 - N_p + B_{12}^* I_1\left(k^*\frac{r}{a}\right)\frac{1}{r}c_1 + B_{12}^* K_1\left(k^*\frac{r}{a}\right)\frac{1}{r}c_2 \\ +(A_{11}+A_{12})c_3 - (A_{11}-A_{12})\frac{1}{r^2}c_4 & x>0 \\ \quad + \frac{1}{2}(B_{11}+B_{12})\frac{pa^2}{D_{11}^* k^{*2}}, \\ -N_p + (B_{11}+B_{12})c_1 - (B_{11}-B_{12})\frac{1}{r^2}c_2 \\ \quad + (A_{11}+A_{12})c_3 & x=0 \\ -(A_{11}-A_{12})\frac{1}{r^2}c_4 - B_{12}^*\frac{1}{16}\frac{pr^2}{D_{11}^*}, \\ N_0 - N_p + B_{12}^* J_1\left(k^*\frac{r}{a}\right)\frac{1}{r}c_1 + B_{12}^* Y_1\left(k^*\frac{r}{a}\right)\frac{1}{r}c_2 \\ \quad + (A_{11}+A_{12})c_3 & x<0, \\ -(A_{11}-A_{12})\frac{1}{r^2}c_4 - \frac{1}{2}(B_{11}+B_{12})\frac{pa^2}{D_{11}^* k^{*2}}, \end{cases} \tag{38}$$

and

$$M_r(r) = \begin{cases} M_0 - M_p + \left[\frac{D_{11}^* k^*}{a} I_0\left(k^*\frac{r}{a}\right) - (D_{11}^* - D_{12}^*) I_1\left(k^*\frac{r}{a}\right)\frac{1}{r}\right]c_1 \\ -\left[\frac{D_{11}^* k^*}{a} K_0\left(k^*\frac{r}{a}\right) + (D_{11}^* - D_{12}^*) K_1\left(k^*\frac{r}{a}\right)\frac{1}{r}\right]c_2 & x>0 \\ +(B_{11}+B_{12})c_3 - (B_{11}-B_{12})\frac{1}{r^2}c_4 \\ \quad + \frac{1}{2}(D_{11}+D_{12})\frac{pa^2}{D_{11}^* k^{*2}}, \\ M_0 - M_p + (D_{11}+D_{12})c_1 - (D_{11}-D_{12})\frac{1}{r^2}c_2 \\ \quad + (B_{11}+B_{12})c_3 & x=0 \\ -(B_{11}-B_{12})\frac{1}{r^2}c_4 - (3D_{11}^* + D_{12}^*)\frac{1}{16}\frac{pr^2}{D_{11}^*}, \\ M_0 - M_p + \left[\frac{D_{11}^* k^*}{a} J_0\left(k^*\frac{r}{a}\right) - (D_{11}^* - D_{12}^*) J_1\left(k^*\frac{r}{a}\right)\frac{1}{r}\right]c_1 \\ +\left[\frac{D_{11}^* k^*}{a} Y_0\left(k^*\frac{r}{a}\right) - (D_{11}^* - D_{12}^*) Y_1\left(k^*\frac{r}{a}\right)\frac{1}{r}\right]c_2 & x<0. \\ +(B_{11}+B_{12})c_3 - (B_{11}-B_{12})\frac{1}{r^2}c_4 \\ \quad - \frac{1}{2}(D_{11}+D_{12})\frac{pa^2}{D_{11}^* k^{*2}}, \end{cases} \tag{39}$$

Because the inner and outer domains can each take on three different solutions depending on the state of in-plane stress (tension, none, compression), a total of nine piecewise analytical solutions are required to account for all the combinations. The algebra associated with such an analytical approach is tedious and the final expressions long; a matrix solution approach is taken here instead. To apply the method, each boundary condition is first written in the form

$$\boldsymbol{C_i^{(1)^T} c^{(1)}} + f_i^{(1)} = \boldsymbol{C_i^{(2)^T} c^{(2)}} + f_i^{(2)}, \tag{40}$$

where each $\boldsymbol{C_i^{(j)}}$ is an array which contains the coefficients of the integration constants, $\boldsymbol{c^{(j)}}$ contains the integration constants themselves, and $f_i^{(j)}$ represents the collected free terms for the ith boundary condition ($i = 1, 2 \ldots 8$) in the jth domain ($j = 1,2$). Collecting the eight equations represented by (40) into a single matrix equation gives

$$\underset{8x3}{\left[-\boldsymbol{C^{(1)}}\right]} \quad \underset{8x5}{\boldsymbol{C^{(2)}}} \begin{Bmatrix} 3x1 \\ \boldsymbol{c^{(1)}} \\ \boldsymbol{c^{(2)}} \\ 5x1 \end{Bmatrix} = \underset{8x1}{\boldsymbol{f^{(1)}}} - \underset{8x1}{\boldsymbol{f^{(2)}}}. \tag{41}$$

The utility of (41) is that the integration constants are found in a modular manner that allows for the coupled solution of any inner region case ($x^{(1)} = -1, 0, 1$) and any outer region case ($x^{(2)} = -1, 0, 1$) simply via matrix inversion of the combined $[C]$ matrix. It is left as an exercise for the reader to derive the integration coefficients and forcing functions appropriate for the three states of in-plane stress (tension, none, compression) for the inner and outer diaphragm regions.

Deflection of the diaphragm occurs due to any or all of 3 inputs: initial stress, pressure, or voltage. In the case of an initially stressed diaphragm, there is an existing static deflection before the application of voltage or pressure. Voltage or pressure loading leads to an additional incremental deflection which in the context of lumped element modeling is the quantity of interest. It is thus convenient to solve for the incremental deflection directly. This is made possible via dividing the array of forcing terms, $\boldsymbol{f^{(j)}}$, into its components,

$$\boldsymbol{f^{(j)}} = \boldsymbol{f_0^{(j)}} + \boldsymbol{f_p^{(j)}} + \boldsymbol{f_v^{(j)}}, \tag{42}$$

where each of $\boldsymbol{f_0^{(j)}}$, $\boldsymbol{f_p^{(j)}}$, and $\boldsymbol{f_v^{(j)}}$ include only those terms relating to in-plane stress, pressure, and voltage, respectively, with all others zero. To solve for the initial deflection alone, replace $\boldsymbol{f^{(j)}}$ with only the in-plane component, $\boldsymbol{f_0^{(j)}}$ (equivalent to letting $v = p = 0$). To solve for the incremental deflection directly, replace the total $\boldsymbol{f^{(j)}}$ by $\boldsymbol{f_p^{(j)}}$ or $\boldsymbol{f_v^{(j)}}$ for incremental deflection due to pressure or voltage, respectively. In these latter cases, the in-plane stress still affects the stiffness via its inclusion in $\boldsymbol{C}$.

3. Experimental results

In this section, measurements of an AlN-based microphone [15, 16] are compared with the analytical solution with and without film stress. Fabrication was performed by Avago Technologies in Fort Collins, CO, using a variant of their film bulk acoustic resonator (FBAR) process [35–38]. The cross-section with geometric dimensions is shown in figure 4. The

device consisted of a borosilicate glass (BSG) structural layer, molybdenum (Mo) electrodes, an AlN piezoelectric layer, and a BSG passivation layer.

During the fabrication, wafer curvature was measured with a Tencor Flexus FLX 5400 after each film deposition and the film stress was estimated using Stoney's Formula [39]. The film stress estimates are collected in table 2 and were used as inputs for the analytical solution with film stress.

Table 2. Diaphragm geometry and stresses in PMUT layers.

Parameter	Thickness (μm)	Stress (MPa)
BSG passivation layer	0.14	−50
Mo top electrode	0.15	−160
AlN piezoelectric layer	1.00	−40
Mo bottom electrode	0.60	10
BSG structural layer	2.00	60

3.1. Initial deflection

A Wyko NT1100 scanning white light interferometer was used to measure the static deflection of the diaphragm. Because AlN is translucent, a thin (50 nm) layer of aluminum was evaporated on the diaphragm to provide a reflective top surface. Two profiles taken at 90 degrees with respect to one another are shown in figure 5 versus the analytical prediction that includes the measured film stresses. There is no bending induced in the zero stress case, such that only the topography of the diaphragm is transcribed. The zero stress diaphragm profile is shown for reference. The experimental and theoretical solutions are well-matched in shape, though the slope of the measurements in the annulus is more pronounced than the theory. This leads to an under-prediction of the center deflection of the diaphragm.

3.2. Pressure loading

The acoustic setup used to measure frontside diaphragm deflection during application of a known oscillatory pressure is shown in figure 6. The device under test (DUT) was mounted in a pressure coupler that allows for exposure to oscillatory pressure on the diaphragm backside. The pressure was measured via a reference microphone at the end of the pressure coupler. The pressures at the DUT and the reference microphone were approximated as equal for low frequency sound where the wavelength was much greater than the distance between the DUT and the reference microphone. The wavelength at 1 kHz (34 cm) was 38 times the test and reference microphone separation and thus more than sufficient to regard the pressures at the two locations as nearly equal. With a resonant frequency greater than 100 kHz, excitation at 1 kHz was sufficiently low to be considered quasi-static. This was confirmed experimentally by placing reference microphones in both locations and measuring the relative pressure while sweeping the excitation frequency. Sound pressure levels from 95 to 105 dB ref 20 μPa were tested. Consistent sensitivity was observed over the pressure range and no measureable harmonics were generated, indicating that the deflection response was within the linear regime.

Vibration measurements were taken over the surface of the diaphragm using a Polytec scanning laser vibrometer (LV) system as shown in figure 6. The experimentally measured deflection per pressure is plotted along with the analytical solutions for the zero stress case and the stress case from table 2 are plotted in figure 7. As is shown in the figure, by not accounting for the film stress, the pressure sensitivity of

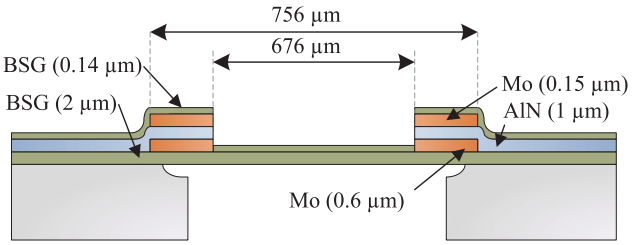

Figure 4. Cross section of the AlN-based microphone with materials and thickness.

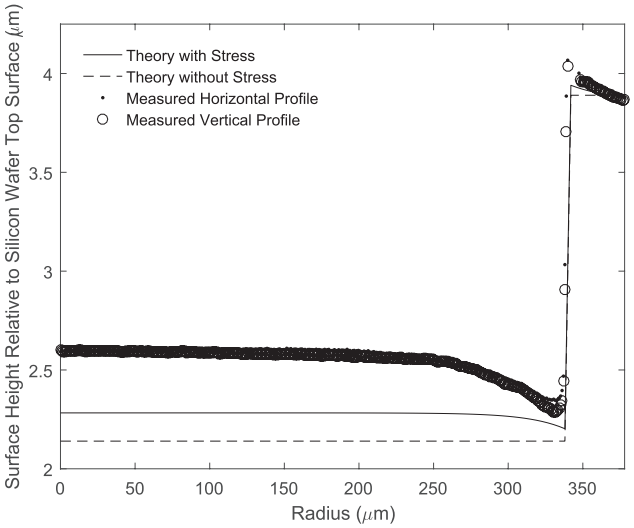

Figure 5. Static deflection of the diaphragm.

the diaphragm is greatly over-predicted. This is to be expected since the net in-plane force from residual stress is positive for both the inner and outer sections of the diaphragm, i.e. x from (23) is positive and the non-dimensional in-plane force parameter k^{*2} (24) is equal to 200 and 12, respectively, for the inner and outer sections. Thus, the residual stress puts the diaphragm in an overall tensile load, increasing it stiffness. By accounting for residual stress, the accuracy of the pressure sensitivity increased by nearly a factor of 10.

3.3. Voltage loading

The diaphragm displacement due to voltage excitation was measured via the experimental setup shown in figure 8. In this instance, an ac voltage was applied to the DUT and the vibration profile was recorded via the Polytec LV. Again, excitation

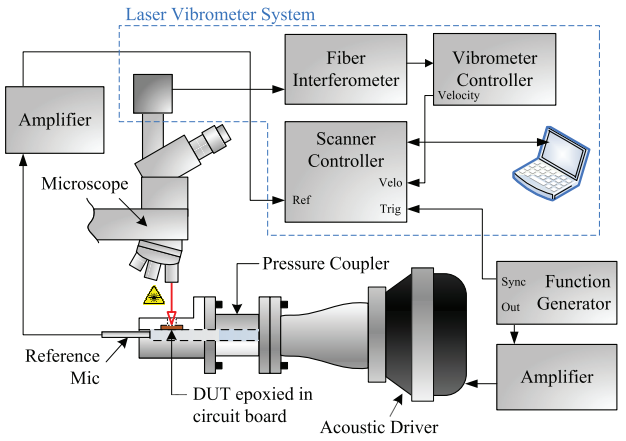

Figure 6. Experimental setup for pressure loading deflection measurements.

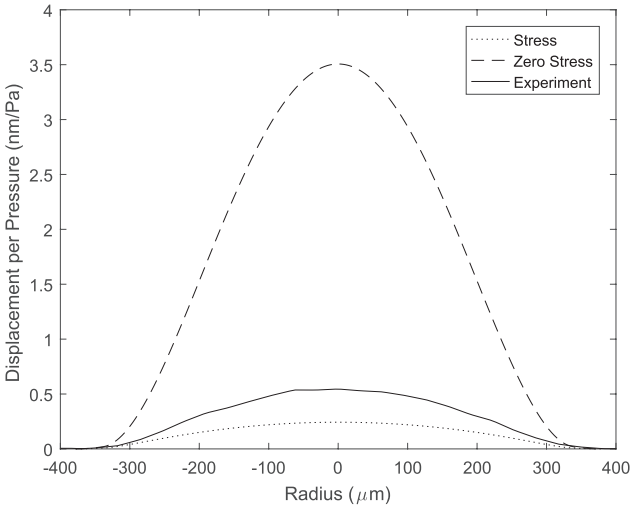

Figure 7. Comparison of the pressure loaded diaphragm deflection profile between the analytical solution accounting for the stress from table 2, the solution neglecting film stress, and the quasi-static results at 1 kHz measured using the experimental setup in figure 6.

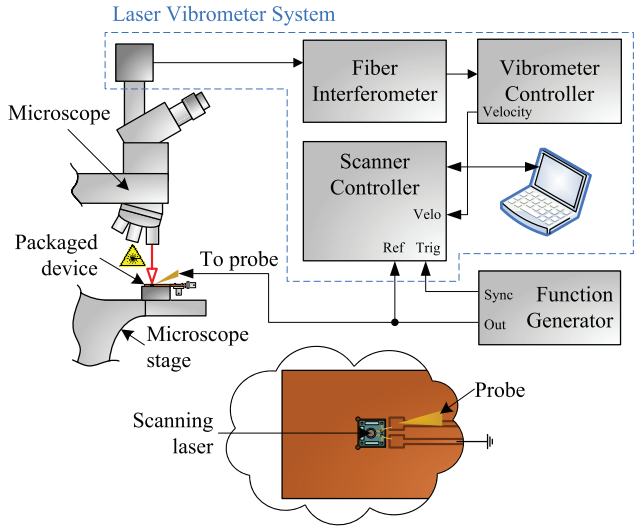

Figure 8. Experimental setup for voltage loading deflection measurements.

at 1 kHz was applied and considered quasi-static. The voltage amplitude for the given results was 2 V. Consistent sensitivity was observed over a range of voltages and no measureable harmonics were generated, indicating that the piezoelectric deflection response was within the linear regime.

The measured deflection profile per voltage is plotted along with the analytical solutions for the zero stress case and the stress case from table 2 in figure 9. Similar to the pressure loading solution, the analytical solution for the zero stress case greatly over-predicts the voltage sensitivity of the overall tensile diaphragm. By accounting for the film stresses, the accuracy of the analytical solution increased by greater than 6 times.

3.4. Stress uncertainty

A Monte Carlo simulation was implemented to assess the effects of uncertainty in the stress measurements. A 12.5 MPa standard deviation was assumed for the stress measurements for each of the films. The mean and standard deviation of the deflections were calculated from sixty-thousand iterations. In addition, an axisymmetric finite element model was developed in COMSOL that incorporates the measured film stresses for comparison. Geometric nonlinearity effects are included in the model to account for large deflections introduced by the film stresses. A parametric solver was used to solve static, pressure-induced, and voltage-induced deflections. The results for pressure and voltage are shown in figures 10 and 11, respectively. The analytical and finite element models show excellent agreement indicating that the combination of geometry and film stresses are in a regime where the linearized analytical model presented is accurate.

The experimental measurements are under-predicted by the two-standard deviation range predicted by the Monte Carlo simulation given the 12.5 MPa standard deviation in each of the film stresses. However, the stress uncertainty reported by Avago Technologies was greater than 50 MPa. At this large of a standard deviation, the Monte Carlo simulation predicted cases where the combination of stresses and geometry put the diaphragm in a buckling regime where the assumptions of the linearized analytical solution are no longer valid. Predicting post-buckled solutions is beyond the scope of the analytical solution presented.

In addition to uncertainty in the stress measurements, a potential bias error exists between the AlN film stress measured at the wafer level and the actual film stress within the diaphragm. Although the film stresses were experimentally measured, they were extracted at the wafer level via wafer bow measurements on films deposited on patterned substrates. As shown in [40], the stress of the AlN film deposited on a patterned bottom electrode will be different than that of the surrounding substrate. Because the patterned bottom electrode is a low percentage of the wafer area, the wafer bow is dominated by the remaining substrate area leading to a bias error between the AlN film stress on the electrode and the film stress measured via wafer bow. Accounting for a bias error in the

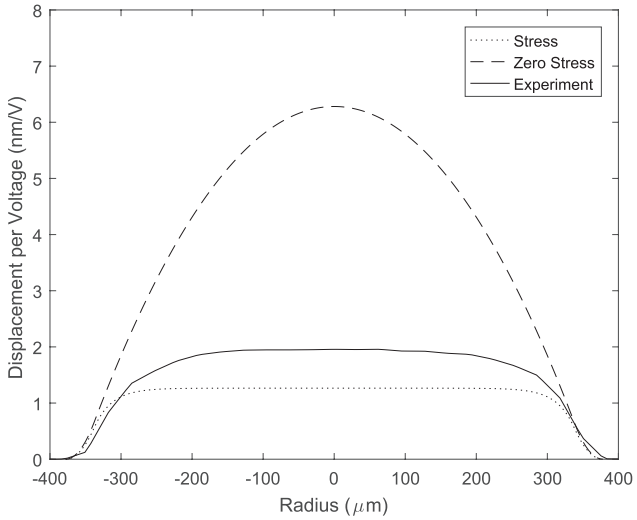

Figure 9. Comparison of the voltage loaded diaphragm deflection profile between the analytical solution accounting for the stress from table 2, the solution neglecting film stress, and the quasi-static results at 1 kHz measured using the experimental setup in figure 8.

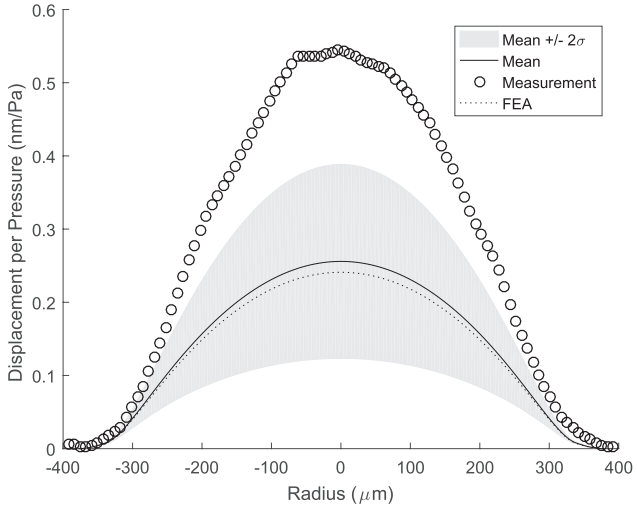

Figure 10. Comparison of the pressure driven diaphragm deflection profile between the measurements using the experimental setup in figure 6, the Monte Carlo simulation using the analytical solution with 12.5 MPa standard deviation in the film stresses, and a COMSOL finite element model simulation incorporating thin film stress.

AlN from −40 MPa to −100 MPa, and shifting the BSG structural layer stress less than one standard deviation from 60 MPa to 25 MPa, the error in the pressure and voltage solutions are reduced to less than 1% as shown in figures 12 and 13. The error in the initial deflection of the diaphragm, as defined in figure 2(b), improved from 69% to less than 22% as shown in figure 14. This underlies the importance of accurate film stress measurements and of films with consistent film stress.

3.5. Results summary

One of the primary benefits of the analytical solution is the efficiency of the computation. This enables the model to be used in a design optimization scheme where the model

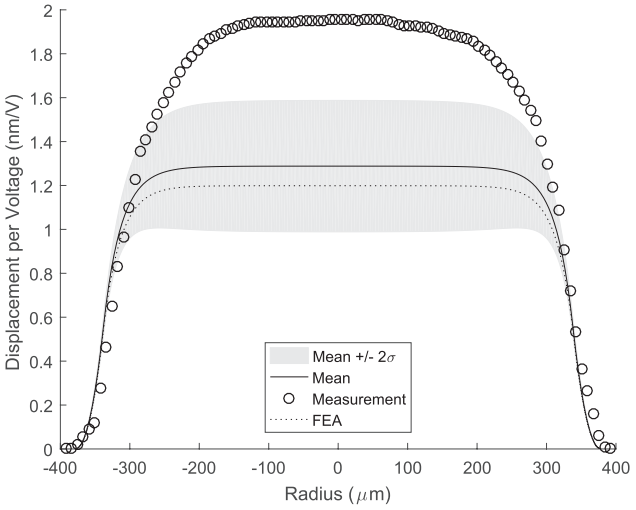

Figure 11. Comparison of the voltage driven diaphragm deflection profile between the measurements using the experimental setup in figure 8, the Monte Carlo simulation using the analytical solution with 12.5 MPa standard deviation in the film stresses, and a COMSOL finite element model simulation incorporating thin film stress.

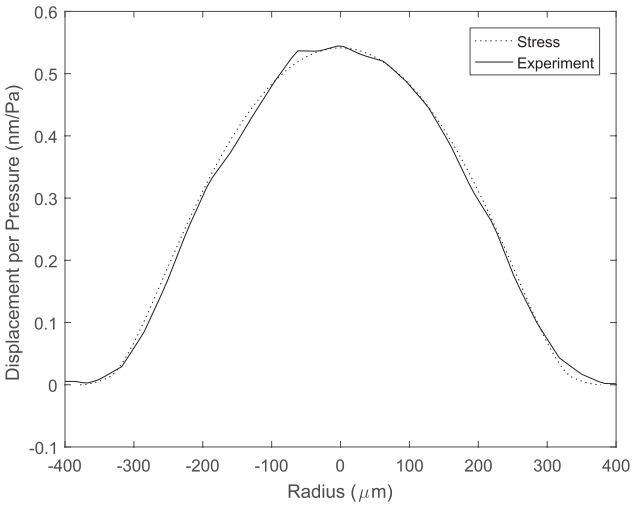

Figure 12. Comparison of the pressure driven diaphragm deflection profile between the measurements and analytical prediction accounting for potential bias error in stress measurement.

calculation is made repetitively. The COMSOL axisymmetric finite element model was used to compare computation speed. A parametric solver was used to solve static, pressure-induced, and voltage-induced deflections. The COMSOL model used 14 500 quadrilateral elements and solved in 22 s. In comparison, the analytical model solved in 80 ms using the same computational hardware.

While there is significant improvement in the prediction of the deflection by including fabrication-induced residual stress, the model does under-predict in comparison to the measured profiles, as shown in figures 10 and 11, likely due to uncertainty in the film stress measurements. The voltage and pressure analytical solutions match to within 35% and 55%, respectively, of the experimentally measured center deflection.

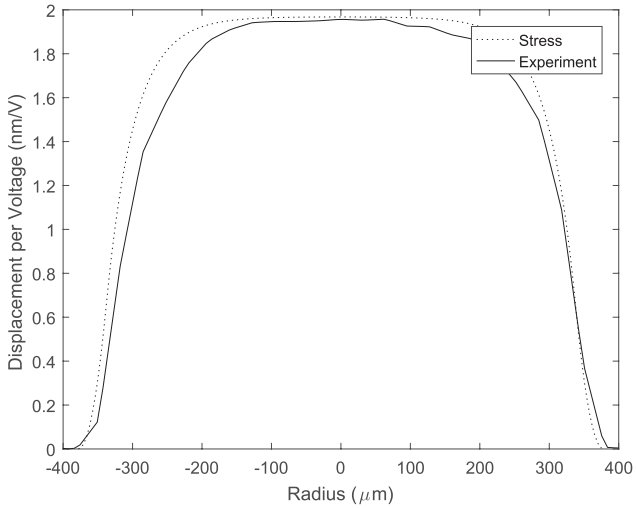

Figure 13. Comparison of the voltage driven diaphragm deflection profile between the measurements and analytical prediction accounting for potential bias error in stress measurement.

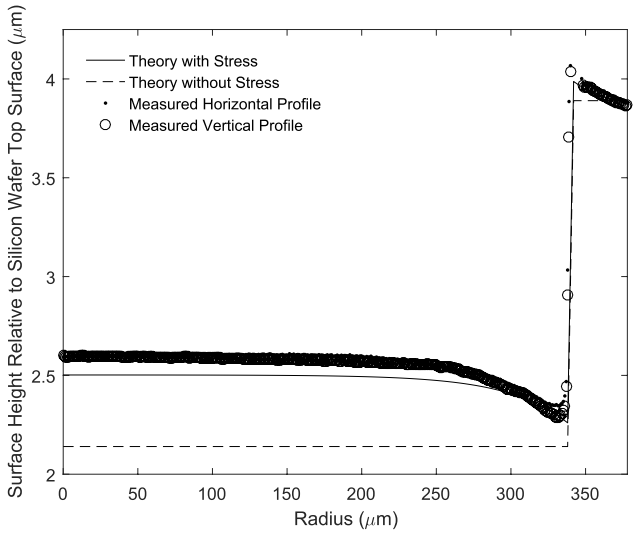

Figure 14. Comparison of the diaphragm topology between the measurements and analytical prediction accounting for potential bias error in stress measurement.

4. Conclusion

In this paper, an analytical model for a radially non-uniform, multi-layered axisymmetric piezoelectric diaphragm subjected to in-plane stresses, transverse pressure, and applied voltage was developed. The model has been used previously along with lumped element modeling to predict the performance of microphone and PMUT devices [9, 15, 16]. Measurements of these devices were compared with theoretical predictions. Inclusion of fabrication-induced residual stress increased the model accuracy by factors of 10 and 6 for the pressure and voltage loading cases, respectively. Deviations between the two were attributed primarily to inaccuracies in measurements of the film stresses used as model inputs. Given accurate inputs, the model is a valuable predictive tool for use in design optimization due to its efficient calculation time.

Acknowledgments

The authors would like to thank Avago Technologies for the microphone fabrication. Matthew D Williams and Benjamin A Griffin would like to acknowledge support from the National Science Foundation for a portion of this study in the form of a pair of Graduate Research Fellowships. Benjamin A Griffin acknowledges additional support by the Laboratory Directed Research and Development (LDRD) program at Sandia National Laboratories. Mark Sheplak acknowledges support from the Boeing Company. Sandia National Laboratories is a multiprogram laboratory managed and operated by Sandia Corporation, a wholly owned subsidiary of Lockheed Martin Corporation, for the US Department of Energy's National Nuclear Security Administration under contract DE-AC04-94AL85000.

References

[1] Horowitz S B, Sheplak M, Cattafesta L N and Nishida T 2006 A MEMS acoustic energy harvester *J. Micromech. Microeng.* **16** S174
[2] Wang L P, Deng K, Zou L, Wolf R, Davis R J and Trolier-McKinstry S 2002 Microelectromechanical systems (MEMS) accelerometers using lead zirconate titanate thick films *IEEE Electron Device Lett.* **23** 182–4
[3] Yu H G, Zou L, Deng K, Wolf R, Tadigadapa S and Trolier-McKinstry S 2003 Lead zirconate titanate MEMS accelerometer using interdigitated electrodes *Sensors Actuators* A **107** 26–35
[4] Koch M, Harris N, Maas R, Evans A G R, White N M and Brunnschweiler A 1997 A novel micropump design with thick-film piezoelectric actuation *Meas. Sci. Technol.* **8** 49–57
[5] Matsumoto S, Klein A and Maeda R 1999 Development of bi-directional valve-less micropump for liquid *Twelfth IEEE Int. Conf. on Microelectromechanical Systems* pp 141–6
[6] Perçin G and Khuri-Yakub B T 2002 Piezoelectrically actuated flextensional micromachined ultrasound transducers *Ultrasonics* **40** 441–8
[7] Muralt P, Ledermann N, Paborowski J, Barzegar A, Gentil S, Belgacem B, Petitgrand S, Bosseboeuf A and Setter N 2005 Piezoelectric micromachined ultrasonic transducers based on PZT thin films *IEEE Trans. Ultrason. Ferroelectr. Freq. Control* **52** 2276–88
[8] Lam T Y, Lam K H and Chan H L W 2005 Micromachined piezoelectric polymer membrane acoustic sensor *Integr. Ferroelectr.* **76** 31–7
[9] Griffin B A, Williams M D, Coffman C S and Sheplak M 2011 Aluminum nitride ultrasonic air-coupled actuator *J. Microelectromech. Syst.* **20** 476–86
[10] Ried R P, Kim E S, Hong D M and Muller R S 1993 Piezoelectric microphone with on-chip CMOS circuits *J. Microelectromech. Syst.* **2** 111–20
[11] Niu M N and Kim E S 2003 Piezoelectric bimorph microphone built on micromachined parylene diaphragm *J. Microelectromech. Syst.* **12** 892–8
[12] Zhao H J, Ren T L, Liu J S, Liu L T and Li Z J 2003 Fabrication of high-quality PZT-based piezoelectric microphone *12th Int. Conf. on Solid-State Sensors, Actuators and Microsystems (Boston, MA) vol* 1 pp 234–7
[13] Horowitz S, Nishida T, Cattafesta L N and Sheplak M 2007 Development of a micromachined piezoelectric microphone for aeroacoustics applications *J. Acoust. Soc. Am.* **122** 3428–36

[14] Lee W S and Lee S S 2008 Piezoelectric microphone built on circular diaphragm *Sensors Actuators* A **144** 367–73
[15] Williams M D, Griffin B A, Reagan T N, Underbrink J R and Sheplak M 2012 An AIN MEMS piezoelectric microphone for aeroacoustic applications *J. Microelectromech. Syst.* **21** 270–83
[16] Williams M D, Griffin B A, Reagan T N, Underbrink J R and Sheplak M 2012 Characterization of aeroacoustic, silicon micromachined microphones for aircraft fuselage arrays *AIAA J.* **50** 2744–52
[17] Madou M 1997 *Fundamentals of Microfabrication* (Boca Raton, FL: CRC Press) pp 261–72
[18] Franssila S 2004 *Introduction to Microfabrication* (Boulder, CO: Wiley) p 401
[19] Antonyak Yu T and Vassergiser M E 1982 Calculation of the characteristics of a membrane-type flexural-mode piezoelectric transducer *Sov. Phys. Acoust.* **28** 176–80
[20] Evseichik Y B, Rudnitskii S I, Sharapov V M and Shul'ga N A 1990 Sensitivity of a metal-piezoceramic bimorph transducer *Int. Appl. Mech.* **26** 1174–81
[21] Chang S H and Du B C 2001 Optimization of asymmetric bimorphic disk transducers *J. Acoust. Soc. Am.* **109** 194–202
[22] Wang G, Sankar B V, Cattafesta L N and Sheplak M 2002 Analysis of a composite piezoelectric circular plate with initial stresses for MEMS *ASME Int. Mechanical Engineering Congress and Exposition (New Orleans, LA)* pp 339–46
[23] Prasad S A N, Gallas Q, Horowitz S, Homeijer B, Sankar B V, Cattafesta L N and Sheplak M 2006 Analytical electroacoustic model of a piezoelectric composite circular plate *AIAA J.* **44** 2311–8
[24] Prasad S A N, Sankar B V, Cattafesta L N, Horowitz S, Gallas Q and Sheplak M 2002 Two-port electroacoustic model of an axisymmetric piezoelectric composite plate *43rd AIAA Structures, Structural Dynamics, and Materials Conf. (Denver, CO)*
[25] Ayela C, Nicu L, Soyer C, Cattan E and Bergaud C 2006 Determination of the d31 piezoelectric coefficient of $PbZr_xTi_{1-x}O_3$ thin films using multilayer buckled micromembranes *J. Appl. Phys.* **100** 054908–9
[26] Li S and Chen S 2003 Analytical analysis of a circular PZT actuator for valveless micropumps *Sensors Actuators* A **104** 151–61
[27] Kim S, Clark W W and Wang Q M 2005 Piezoelectric energy harvesting with a clamped circular plate: analysis *J. Intell. Mater. Syst. Struct.* **16** 847
[28] Mo C, Wright R, Slaughter W S and Clark W W 2006 Behaviour of a unimorph circular piezoelectric actuator *Smart Mater. Struct.* **15** 1094–102
[29] Mo C, Wright R and Clark W W 2007 The effect of electrode pattern on the behavior of piezoelectric actuators in a circular diaphragm structure *J. Intell. Mater. Syst. Struct.* **18** 467
[30] Deshpande M and Saggere L 2007 An analytical model and working equations for static deflections of a circular multi-layered diaphragm-type piezoelectric actuator *Sensors Actuators* A **136** 673–89
[31] Papila M, Sheplak M and Cattafesta L N 2008 Optimization of clamped circular piezoelectric composite actuators *Sensors Actuators* A **147** 310–23
[32] Reddy J N 1999 *Theory and Analysis of Elastic Plates* (Philadelphia, PA: Taylor & Francis) ch 1–3, 5
[33] Nayfeh A H and Pai P F 2004 *Linear and Nonlinear Structural Mechanics* (*Wiley Series in Nonlinear Science*) (Hoboken, NJ: Wiley-Interscience)
[34] Timoshenko S and Woinowsky-Krieger S 1959 *Theory of Plates and Shells* (New York: McGraw-Hill) p 391
[35] Ruby R C, Bradley P, Oshmyansky Y, Chien A and Larson J D 2001 Thin film bulk wave acoustic resonators (FBAR) for wireless applications *Proc. IEEE Ultrasonics Symp.* vol **1** pp 813–21
[36] Fazzio R S, Dauksher W, Goel A and Lamers T L 2007 Analysis of micromachined piezoelectric transducers operating in a flexural mode *Proc. of ASME Int. Mechanical Engineering Congress and Exposition (Seattle, WA, 11–15 November 2007)* pp 339–46
[37] Lamers T L and Fazzio R S 2007 Accelerating development of a MEMS piezoelectric microphone *Proc. of the ASME 2007 Int. Design Engineering Technical Conf. & Computers Information in Engineering Conf. (Las Vegas, NV, 4–7 September 2007)* pp 593–601
[38] Fazzio R S, Lamers T, Buccafusca O, Goel A and Dauksher W 2007 Design and performance of aluminum nitride piezoelectric microphones *14th Int. Conf. on Micro-Sensors, Actuators and Microsystems (Lyon, France, 10–14 June 2007)* pp 1255–8
[39] Stoney G G 1909 The tension of metallic films deposited by electrolysis *Proc. R. Soc.* A **82** 172–5
[40] Choi S and Griffin B A 2016 Local residual stress monitoring of aluminum nitride MEMS using UV micro-Raman spectroscopy *J. Micromech. Microeng.* **26** 025009